Hydrogen and electricity co-generation from hydrazine-assisted water electrolysis on hierarchical porous heteroatoms-doped CoCu catalysts

Shuxian Zhuang [a,b], Yang Tang [a,b,*], Xuefeng Tai [b], Qian Huang [b], Pingyu Wan [a,b,*], Yongmei Chen [b], Yanzhi Sun [b], Junqing Pan [a], Xiao Jin Yang [a,**]

[a] *State Key Laboratory of Chemical Resource Engineering, Beijing University of Chemical Technology, Beijing 100029, China*
[b] *National Fundamental Research Laboratory of New Hazardous Chemicals Assessment & Accident Analysis, Beijing University of Chemical Technology, Beijing 100029, China*

ARTICLE INFO

ABSTRACT

In order to decrease the electricity consumption of water electrolysis, we investigated a novel hydrazine-assisted water electrolysis for electricity-independent hydrogen production, featuring with lower anodic hydrazine oxidation reaction (HzOR) than cathodic hydrogen evolution reaction (HER). The adsorption and semiconductor characteristics of hierarchical porous $Co_{NS}@Cu_{PD}$, interlacing by $Co(OH)_2$ nanosheets on the Cu dendrites surface, are selectively modified to optimize anodic HzOR and cathodic HER performance through doping B and P heteroatoms, respectively. The working potential of HzOR on B-doped $Co_{NS}@Cu_{PD}$ negatively shifts to -146 mV at 10 mA cm^{-2}, while that of HER on P-doped $Co_{NS}@Cu_{PD}$ positively shifts to -70 mV. Consequently, the hydrazine electrolysis device using B-/P-doped catalysts output a small voltage of 60 mV at 10 mA cm^{-2}, achieving co-generation of hydrogen and electricity for the first time. This work brings an intrinsic break in hydrogen-rich molecule-assisted water electrolysis for hydrogen production.

1. Introduction

Hydrogen-based equipment have been widely penetrating into the fields of transportation, energy, military and emergency as a highly efficient energy carrier and source [1,2]. Water electrolysis driven by renewable electricity is a green hydrogen production process [3,4] in which the major challenge is to reduce the cell voltage as low as possible. The cell voltage of water electrolysis has been reduced to 1.5–1.8 V [5–7] relative to the theoretical voltage of 1.23 V and a further reduction is difficult due to the inevitable overpotentials of the hydrogen evolution reaction (HER) and particularly, the oxygen evolution reaction (OER) [8,9]. However, in some field applications with limited or no electricity, such as emergency and military scenes, it is more convenient to carry traditional liquid fuels rather than to find electricity grid or construct microgrid for producing hydrogen. This contradiction hinders the utilization of advantages of hydrogen energy and the development of hydrogen equipment in those fields.

In order to further reduce the cell voltage of water electrolysis for hydrogen generation, an alternative is to replace the OER with the oxidation of liquid hydrogen-rich molecules having favorable thermodynamic potential such as hydrazine (N_2H_4), [10] sodium borohydride ($NaBH_4$), [11] urea (CH_4N_2O) [12] and ammonia borane ($NH_3 \cdot BH_3$) [13]. The hydrazine electrolysis (HzE: $N_2H_4 \rightarrow N_2 + 2H_2$) involves the anodic hydrazine oxidation reaction (HzOR: $N_2H_4 + 4OH^- \rightarrow N_2 + 4H_2O + 4e^-$)[14] and the cathodic HER ($2H_2O + 4e^- \rightarrow H_2 + 2OH^-$) and has an advantage of the electrochemically controllable production of high-purity hydrogen at ambient temperature as compared to the chemical decomposition [15–17]. In principle, the HzE could be operated in a zero cell voltage as the theoretical oxidation potential of hydrazine is -330 mV vs. reversible hydrogen electrode (RHE). However, achieving this has been challenging due primarily to the overpotentials of HzOR and HER. The cell voltage of HzE on leading electrocatalysts has been significantly reduced from 500 to 700 mV [10,18,19] to about 100 mV [20–22] at a current density of 10 mA cm^{-2}. However, external electricity is still required to motivate the N_2H_4-assisted electrochemical hydrogen production system, which strict its application in the

---

electricity-dependent fields. The concept of self-powered H_2 production from HzE was also proposed, which was integrated with solar cells [23], hydrazine fuel cells [15,16] or driven by neutralization energy [24]. However, these integrated systems are not an intrinsically self-powered process, as the HzE in these systems still relies on external electric power (above mentioned cells) or chemical energy. In addition, the integrated systems are complicated, hindering the practical applications.

The intrinsically self-powered HzE should have a lower working potential for anodic HzOR than cathodic HER, which requests sufficiently low overpotentials of them. Notably, the appropriate adsorption and dissociation of N_2H_4, H_2O and other intermediates would contribute to efficient anodic and cathodic performance, respectively [17,25]. Recently, tremendous investigations have been carried to decrease the overpotentials of both HzOR and HER by modifying absorption characteristics for N_2H_4 and H_2O on the surface of catalysts, and HzE voltage has been decreased to 71–28 mV on those well-designed bifunctional electrocatalysts [15,26,27]. Eminently, Li et al. [28] reported the partially exposed RuP_2 nanoparticle decorated carbon porous microsheets fabricated by one-pot synthesis method, in which the exposed RuP_2 as active sites for HzOR and carbon layer facilitates HER. The HzE voltage in this work is greatly reduced to 23 mV@10 mA cm^{-2}, the lowest value reported previously. However, limited by polarization effect, it is impossible to realize the lower anodic potential than cathodic potential on those bifunctional electrocatalysts.

Herein, we proposed to selectively modify the electronic structure of a tailored CoCu catalyst with hierarchical porous structure through B and P doping to regular its adsorption and semiconductive characteristics in an opposite direction (Scheme 1). This strategy down shifts the HzOR potential and up shifts the HER potential selectively, thereby intrinsically achieving a lower working potential for HzOR than HER and co-generation of H_2 and electricity by hydrazine-assisted water electrolysis (Scheme 1). Density functional theory (DFT) calculations confirmed the effects of different heteroatom doping on the adsorption characteristics of the catalyst surface. Moreover, the unique hierarchical porous structure of the catalyst provides an electron-express way which cooperate to facilitate the adsorption, dissociation and electron transfer of HzOR and HER reactions. The truly self-powered HzE at electricity-

free conditions provides a novel and feasible solution for co-generation of hydrogen and electricity in the off-grid environment.

2. Experimental

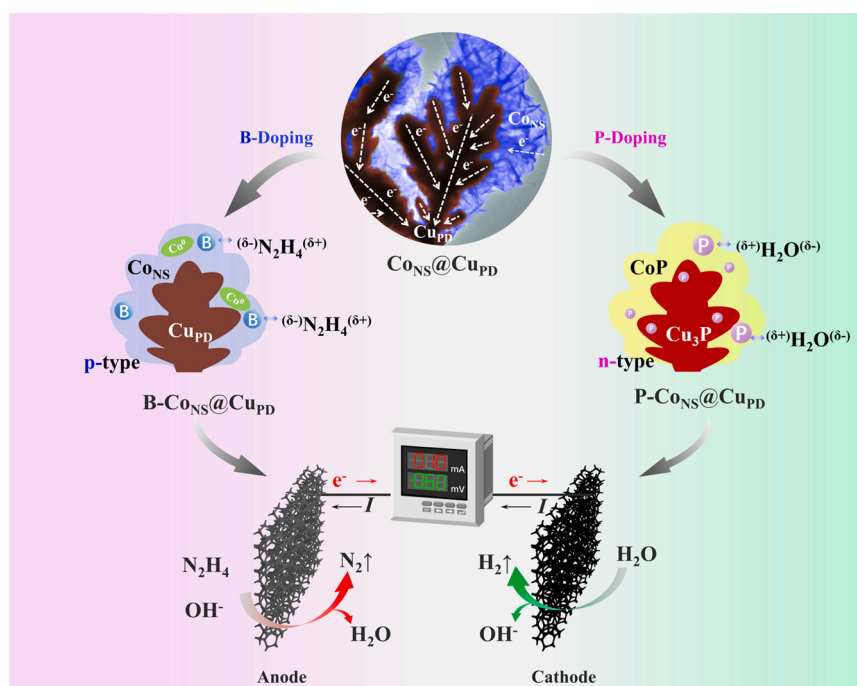### 2.1. Synthesis of Cu_{PD}, Co_{NS} and $Co_{NS}@Cu_{PD}$ electrodes

The Ni foam substrate (NF, 1×1 cm^2) was in sequence sonicated in acetone, 0.1 M KOH, 0.5 M HCl and ultrapure water to remove surface oil and native oxide layer, and then dried in air naturally. The microporous dendritic Cu_{PD} electrode was synthesized at a cathodic current density of -4 A cm^{-2} for 20 s, using the treated NF as working electrode and the commercial RuO_x/Ti electrode as counter electrode. The electrodeposition solution is composed of 0.2 M $CuSO_4 \cdot 5H_2O$, 1.5 M $(NH_4)_2SO_4$, 1 mM BTA and 3 M H_2SO_4. The Co_{NS} and $Co_{NS}@Cu_{PD}$ electrodes was synthesized at -1 V (vs. saturated calomel electrode (SCE)) for 60 s in 0.15 M $Co(NO_3)_2 \cdot 6H_2O$, using NF and Cu_{PD} as working electrode, respectively. Ar was bubbled continuously to remove dissolved oxygen before and during electrodeposition process.

2.2. Synthesis of $B-Co_{NS}@Cu_{PD}$ and $P-Co_{NS}@Cu_{PD}$ electrodes

The B-doped $Co_{NS}@Cu_{PD}$ was prepared by a facile electrochemical cyclic voltammetry treatment at the range of -0.2 to 0 V (vs. reversible hydrogen electrode (RHE)) for 10 cycles in 1 M NaOH-0.05 M $NaBH_4$ at room temperature. The obtained $B-Co_{NS}@Cu_{PD}$ electrode was rinsed with ultrapure water several times and dried in air naturally. On the other hand, the $Co_{NS}@Cu_{PD}$ electrode was put into a porcelain boat at the center of tube furnace, and NaH_2PO_2 were put into another porcelain boat at the upstream of tube. The tube furnace was then heated to 300 °C at the rate of 5 °C min^{-1} and hold for 2 h under Ar atmosphere. The $P-Co_{NS}@Cu_{PD}$ electrode was obtained after the naturally cooling to room temperature.

2.3. Characterization

Scanning electron microscopy (SEM) measurement was carried out

Scheme 1. Schematic illustration of doping B into $Co_{NS}@Cu_{PD}$ for preferred adsorption of N_2H_4 and doping P for adsorption of H_2O, and their application in the two-electrode system of hydrazine-assisted water electrolysis for co-generation of hydrogen and electricity.

on a Zeiss Supra 55, with energy-dispersive spectrometer (EDS) and element mapping analysis. High-resolution transmission electron microscopy (HRTEM) measurement was performed on a JEM-2100. X-ray photoelectron spectroscopy (XPS) measurement was carried out on a ESCALAB 250Xi XPS spectrometer with a monochromate Al Kα X-ray source. X-ray diffraction (XRD) pattern was recorded on a Rigaku D/max 2500 diffractometer and Shimadzu XRD-6100 diffractometer with Cu Kα radiation (λ = 0.15418 nm) from 5° to 90°.

2.4. Electrochemical measurements

All electrochemical measurements were performed using CHI 760E electrochemical workstation at room temperature in the standard three-electrode system with SCE as reference electrode, and commercial RuO_x/Ti electrode as counter electrode. The Cu_{PD}, Co_{NS}, $Co_{NS}@Cu_{PD}$, B-$Co_{NS}@Cu_{PD}$, P-$Co_{NS}@Cu_{PD}$, S-$Co_{NS}@Cu_{PD}$, NF, Powder Drop-coating electrode and commercial Pt/C were employed as working electrodes. Both HzOR and HER were tested by linear sweep voltammetry (LSV), chronopotentiometry, Tafel in 3 M KOH-0.1 M N_2H_4.

All the potentials mentioned in this work were calibrated with respect to RHE. The potential calibration was performed in H_2-saturated 3 M KOH-0.1 M N_2H_4 using the Pt wire electrode as working electrode. The cyclic voltammograms (CV) curve with a slow scan rate of 1 mV s^{-1} was shown in Fig. S1. It can be observed that the current reaches zero at − 1.088 V respect to SCE. The potential can be calibrated to RHE in the following equation: E (RHE) = E (SCE) + 1.088 V. And the potentials were recorded with 80% iR-compensation.

2.5. Density function theory (DFT) calculations

We have employed the first-principles [29,30] to perform density functional theory (DFT) calculations within the generalized gradient approximation (GGA) using the Perdew-Burke-Ernzerhof (PBE) [31] formulation. We have chosen the projected augmented wave (PAW) potentials [32,33] to describe the ionic cores and take valence electrons into account using a plane wave basis set with a kinetic energy cutoff of 400 eV. Partial occupancies of the Kohn-Sham orbitals were allowed using the Gaussian smearing method and a width of 0.05 eV. The electronic energy was considered self-consistent when the energy change was smaller than 10^{-6} eV. A geometry optimization was considered convergent when the energy change was smaller than 0.05 eV Å^{-1}. In addition, for the Co atoms, the U schemes need to be applied, and the U has been set as 4.7 eV. And spin correction has been considered in our system. In the process of simulating crystal surface calculation, to avoid repetition for surface interaction, the distance of vacuum spacing in discontinuous direction was 13 Å. In all the calculation, we use $3 \times 3 \times 1$ for the Monkhorst-Pack k-point for periodic interface model. During the process of intermediate state optimization, the substrate is fixed to simulation the reality situation. The free energy was calculated using the equation:

$$G = E + ZPE + TS$$

where G, E, ZPE and TS represented the free energy, total energy from DFT calculations, zero-point energy and entropic contributions (T was set to be 300 K), respectively [34].

In order to simplify the construction of atomic models, combining the characterization results, the atomic structure model of $Co_{NS}@Cu_{PD}$ consists of $Co(OH)_2$ on the upper area and metallic Cu on the lower area; the metallic Co (reduced by $NaBH_4$) was added in to the atomic structure model of B-$Co_{NS}@Cu_{PD}$ based on that of $Co_{NS}@Cu_{PD}$, and the B atom was introduced into the $Co(OH)_2$ crystal lattice; the atomic structure model of P-$Co_{NS}@Cu_{PD}$ consists of CoP on the upper area and Cu_3P on the lower area. For the three materials, the adsorption sites are respectively selected on the Co planes of $Co(OH)_2$ (0 0 1), Co (1 1 1) and CoP (2 1 1) respectively.

3. Results and discussion

3.1. Characterization of hierarchical porous CoCu catalyst

A thin layer of microporous Cu was coated on the surface of NF by electrodeposition using in-situ generated vigorous hydrogen bubbles as the dynamic template and named as Cu_{PD} (Fig. 1a).[35,36] As shown in Fig. S2a-d (SEM images of NF and Cu_{PD}), a relatively regular distribution of micropores (15–25 μm) is observed on the surface of Cu coating (Fig. S2b) which formed by the clusters of porous dendritic Cu (Fig. S2d). The electrodeposition of $Co(OH)_2$ onto Cu_{PD} does not alter the surface morphology (Fig. 1a and Fig. S2e-g) and the dendritic structure (Fig. 1b and Fig. S2f) of the Cu coatings, thus creating a micro-nano hierarchical porous structure of $Co(OH)_2$ nanosheets on Cu dendrites ($Co_{NS}@Cu_{PD}$). By contrast, the electrodeposition of Co on NF produces nanosheet arrays (Co_{NS}) (Fig. S2h-j). The $Co_{NS}@Cu_{PD}$ contains Cu^0 and $Co(OH)_2$ as evidenced by HRTEM characterization (Fi. 1c, d) and the XPS spectra (Fig. 1f, g). The SEM image and its corresponding line-scanning image (Fig. 1e) clearly demonstrate the elements distribution of the CoCu catalyst. In XRD pattern (Fig. S3), the strong diffraction peaks are assigned to metallic Ni from NF and metallic Cu from microporous dendritic Cu. Besides, the three weak peaks at about 10.9°, 21.6° and 33.7° could be attributed to the characteristic diffraction peaks of typical $Co(OH)_2$.

The electrocatalytic activity of Pt/C, NF, Cu_{PD}, Co_{NS} and $Co_{NS}@Cu_{PD}$ towards HzOR and HER was investigated using a typical three-electrode system in 3 M KOH-0.1 M N_2H_4 (Fig. 2a, b). Coating metallic, microporous Cu on NF improves HzOR performance of Cu_{PD} significantly whereas Co_{NS} with $Co(OH)_2$ nanosheets coating on NF does not show appreciate HzOR activity (Fig. 2a). $Co_{NS}@Cu_{PD}$ is the best HzOR electrocatalyst showing the lowest onset potential of − 136 mV (Fig. 2a), the lowest working potential of − 124 mV at a current density of 10 mA cm^{-2} and the smallest Tafel slope of 28.2 mV Dec^{-1} (insert in Fig. 2a). Moreover, $Co_{NS}@Cu_{PD}$ exhibits a much lower charge transfer resistance (R_{ct}) of ~1 Ω (Fig. S4) which means that it possesses great electronic transfer ability, contributing to a higher catalytic activity. For comparison, the NF electrodes coated with $Co(OH)_2$ or/and Cu powder (named as Co_p, Cu_p, Co_p @Cu_p, synthesis method in Supporting Information) were also investigated (Fig. S5). Clearly, $Co_{NS}@Cu_{PD}$ displays much higher catalytic activity towards HzOR than Co_p, Cu_p and Co_p @Cu_p. This indicates the importance of the hierarchical porous structure to the HzOR activity. To the best of our knowledge, $Co_{NS}@Cu_{PD}$ exhibits much better HzOR activity than any other Cu- and/or Co-based electrocatalysts reported in the literature (Fig. S6 and Table S1). Interestingly, $Co_{NS}@Cu_{PD}$ also shows significantly higher HER activity than NF, Cu_{PD} and Co_{NS} and delivers a current density of − 10 mA cm^{-2} towards HER at an overpotential of 166 mV, which is significantly lower than NF's 311 mV, Cu_{PD}'s 255 mV and Co_{NS}'s 284 mV (Fig. 2b, c). The HzOR and HER working potential (E_{HzOR} and E_{HER}) on Pt/C, NF, Co_{NS}, Cu_{PD} and $Co_{NS}@Cu_{PD}$ at ± 10 mA cm^{-2} are shown in Fig. 2c. Calculating from these results, the overpotentials of both HzOR and HER (η_{HzOR} and η_{HER}) are in the order of NF < Co_{NS} < Cu_{PD} < $Co_{NS}@Cu_{PD}$. Notably, the value of E_{HzOR}-E_{HER} on $Co_{NS}@Cu_{PD}$ is only 42 mV compared to 73 mV on the current state-of-the-art Pt/C electrocatalyst. This value reflects the cell voltage required for a two-electrode device to electrochemically split hydrazine and it could be minimized to zero or even less than zero if η_{HzOR} and η_{HER} were further reduced.

As verified by the electrochemical specific area (ECSA) measurement (Fig. S7), $Co_{NS}@Cu_{PD}$ exhibits huge specific surface areas (430 cm^2), thanks to perpendicularly grown and interlaced $Co(OH)_2$ nanosheets on the surface of microporous dendritic Cu, which would facilitate the expose of active sites and gas diffusion and thus promote catalytic performance [37]. On the other hand, the surface conductivity also strongly correlates with the electrocatalytic activity of a semiconductor catalyst [38]. Both sides of the $Co(OH)_2$ nanosheets are likely to rapidly transport electrons from dendritic Cu to the electrolyte thus minimizing the
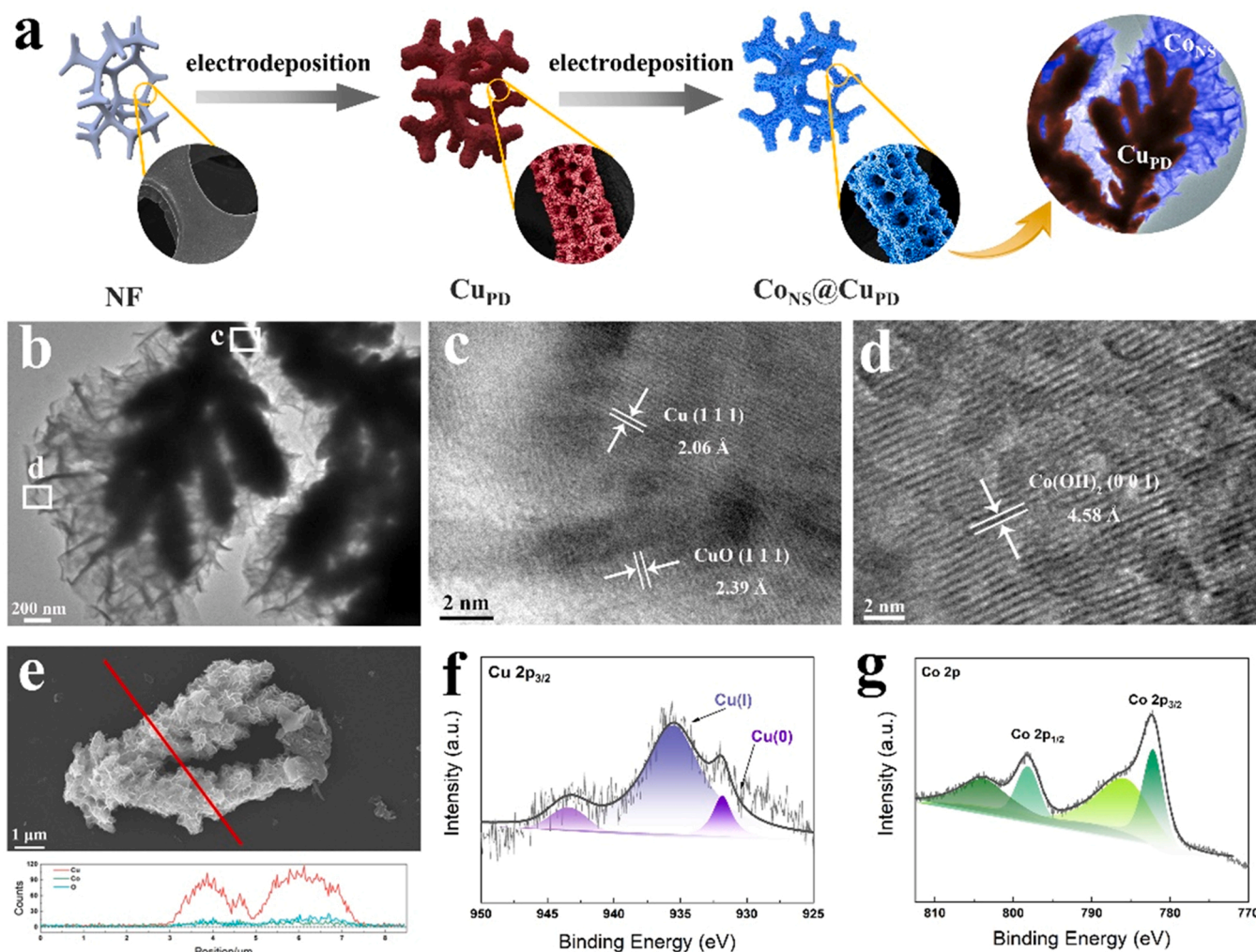
Fig. 1. (a) Schematic illustration of preparation process of Cu_{PD} and $Co_{NS}@Cu_{PD}$ with hierarchical porous structure. (b) TEM and (c, d) HRTEM images, (e) corresponding line-scanning of Cu, Co and O, (f) Cu 2p and (g) Co 2p XPS spectra for $Co_{NS}@Cu_{PD}$.

accumulation of electrons at the catalyst-electrolyte interface and improving the conductivity (refer to Fig. 2d). Moreover, the positively charged Co^{2+} sites in the topmost $Co(OH)_2$ nanosheets improve the affinity with OH^- and N_2H_4 facilitating the kinetics of HzOR [39,40]. The intrinsic activity towards HzOR were further estimated through normalizing LSV curves of ECSA and mass loading amount [41]. The specific HzOR current density of $Co_{NS}@Cu_{PD}$ electrode is higher than that of NF, Cu_{PD} and Co_{NS} (Fig. S8a), which further explain that the synergistic effect from CuCo composites and hierarchical porous structure are vital to enhance catalytic performance. The mass activity towards HzOR of $Co_{NS}@Cu_{PD}$ is also highest among above electrodes (Fig. S8b). All the normalized results suggest the highest intrinsic catalytic activity of $Co_{NS}@Cu_{PD}$.

In spite of the exceptional performance of the $Co_{NS}@Cu_{PD}$ as a bifunctional catalyst for HzOR and HER mentioned above, the working potential of HzOR is still higher than that of HER (see Fig. 2c). Therefore, we proposed the modulation of the surface electronic state in an opposite direction ("push and pull") to further reduce the overpotentials of HzOR and HER, achieving $E_{HzOR} < E_{HER}$. Zhang and his co-workers [38] observed that the p-type semiconductor catalysts preferred anodic reactions (e.g., OER) while the n-type semiconductor catalysts favored cathodic reactions (e.g., HER). It arouses us that the construction of different semiconductor characteristic on the catalysts surface may be the efficient way to reduce the overpotentials of HzOR and HER respectively.

3.2. B-doping for HzOR and P-doping for HER

$Co_{NS}@Cu_{PD}$ was doped with B and P, respectively denoted as B-$Co_{NS}@Cu_{PD}$ and P-$Co_{NS}@Cu_{PD}$. The EDX mapping results indicated that B and P were successfully doped into the catalysts and that there was a uniform distribution of Co, Cu and B or P in B-$Co_{NS}@Cu_{PD}$ and P-$Co_{NS}@Cu_{PD}$ (Fig. 3a, e and Table S2). The hierarchical microporous structure of $Co_{NS}@Cu_{PD}$ was well maintained after B and P doping (refer to Fig. S9). Nevertheless, the $Co(OH)_2$ nanosheets became rougher and slightly thicker after B doping (Fig. 3b) while the $Co(OH)_2$ nanosheets became more curved and slightly smaller after P doping by high-temperature treatment (Fig. 3f). According HRTEM images and XRD patterns, B-$Co_{NS}@Cu_{PD}$ contained Cu (2 0 0) and Co (1 1 1) planes (Fig. 3c-d) while Cu_3P and CoP were identified on the surface of P-$Co_{NS}@Cu_{PD}$ (Fig. 3g–h and Fig. S10).

The XPS survey spectra of $Co_{NS}@Cu_{PD}$, B-$Co_{NS}@Cu_{PD}$ and P-$Co_{NS}@Cu_{PD}$ are shown in Fig. 4a. In the B 1s spectrum (Fig. 4b), the two peaks at 183.36 and 186.44 eV belong to B 1s in the chemical state of B^0 and the other peak at 191.93 eV is in the chemical state of B^{3+} [42]. In the P 2p spectrum (Fig. 4c), the two peaks at 129.32 eV and 130.25 eV correspond to $2p_{3/2}$ and $2p_{1/2}$ of $P^{\delta-}$ respectively, while another strong peak at 134.39 eV belongs to P-O species. After B-doping, the occurrence of a strong Cu^0 peak (Fig. 4d) indicates that some of the Cu oxides are converted into metallic Cu due to the reduction by $NaBH_4$. On the other hand, B-doping negatively shifts the Co $2p_{3/2}$ and $2p_{1/2}$ peaks by 0.46 eV
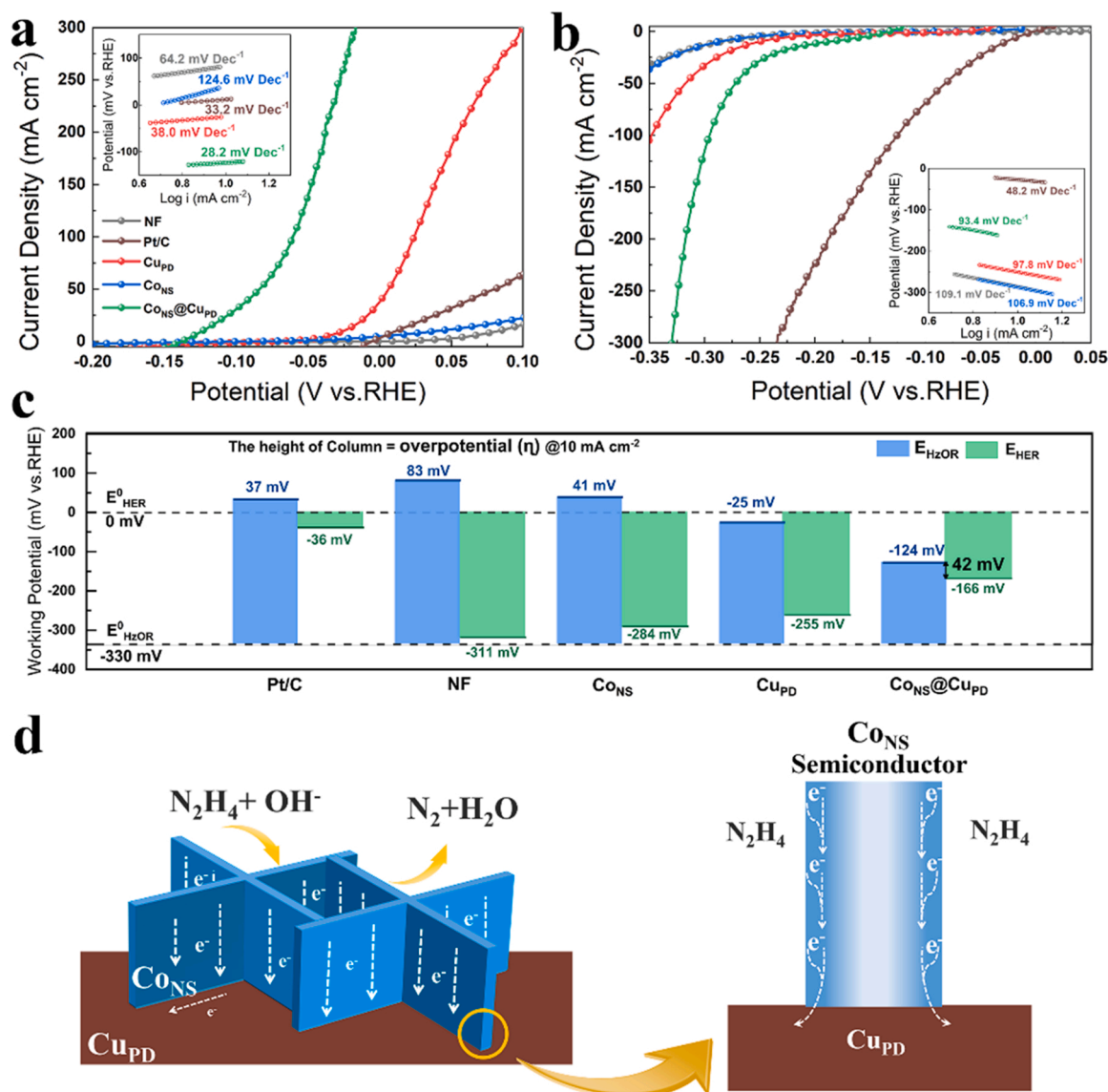
Fig. 2. (a) HzOR and (b) HER LSV curves of Pt/C, NF, Co_{NS}, Cu_{PD} and $Co_{NS}@Cu_{PD}$ at a scan rate of 5 mV s^{-1} in 3 M KOH-0.1 M N_2H_4. The insets in (a) and (b) are the Tafel slopes calculated from the corresponding HzOR and HER LSV curves. (c) The working potentials of above electrodes towards the anodic HzOR (blue) and the cathodic HER (green) at a constant current density of 10 mA cm^{-2}. (d) Schematic illustration of $Co(OH)_2$ nanosheets interlacing on Cu_{PD} and electron transfer from N_2H_4 to Cu_{PD} at the interface.

and 0.71 eV, respectively (Fig. 4e). Therefore, the doped B provides electrons for both Cu oxides and $Co(OH)_2$ and redistributes the surface electrons of $Co_{NS}@Cu_{PD}$. Doping B into Co-based catalysts can create electron-deficient B sites, [43,44] which are favored to adsorb Lewis bases (*N_2H_x) and repel Lewis acids (protons) [45,46]. In this context, doping B into $Co_{NS}@Cu_{PD}$ could improve HzOR and suppress HER. After P-doping, typical peaks of Cu_3P and CoP were observed (Fig. 4c–e) [47]. The peaks for Cu 2p$_{3/2}$ (932.84 eV) and Co 2p$_{3/2}$ (778.63 eV) were positively shifted relative to metallic Cu (931.86 eV) and Co (778.10–778.20 eV) while the P 2p$_{3/2}$ peak (129.31 eV) was negatively shifted compared to elemental P (130.10 eV) [48,49]. These observations demonstrate that the electrons are transferred from Cu and Co to P and that the electron-acceptor P$^{\delta-}$ tends to attract protons and promote HER process [50].

Fig. S11 and Fig. 5a show the Mott-Schottky analysis results for $Co_{NS}@Cu_{PD}$, B-$Co_{NS}@Cu_{PD}$ and P-$Co_{NS}@Cu_{PD}$ tested in a typical three-electrode system. The negative slope of Mott-Schottky curve for $Co_{NS}@Cu_{PD}$ indicates its p-type semiconductor characteristic on the surface. Afterwards, the negative and positive slopes of the Mott-Schottky curves

prove the p- and n-type semiconductor characteristics [51,52] for B-$Co_{NS}@Cu_{PD}$ and P-$Co_{NS}@Cu_{PD}$, respectively. Consequently, doping B into $Co_{NS}@Cu_{PD}$ enhanced the anodic HzOR while doping P improved the cathodic HER significantly (Fig. 5b). The HzOR onset potential was − 136 mV on $Co_{NS}@Cu_{PD}$ in 3 M KOH-0.1 M N_2H_4 and it negatively shifted to − 156 mV after B-doping and positively shifted to − 61 mV after P-doping. The anodic current density on B-$Co_{NS}@Cu_{PD}$ increased more quickly than that on $Co_{NS}@Cu_{PD}$ with increasing potential. Specifically, $Co_{NS}@Cu_{PD}$ and B-$Co_{NS}@Cu_{PD}$ reached 57 and 300 mA cm^{-2} for HzOR respectively at a very negative potential of − 79 mV, while HzOR did not initiate on P-$Co_{NS}@Cu_{PD}$ at the identical potential. And both B-$Co_{NS}@Cu_{PD}$ and $Co_{NS}@Cu_{PD}$ show significantly reduced working potential for HzOR as compared with OER, indicating that replacing OER by HzOR efficiently decrease the anodic potential of water electrolysis (Fig. S12). Nevertheless, P-$Co_{NS}@Cu_{PD}$ exhibited significantly higher HER current than $Co_{NS}@Cu_{PD}$ and B-$Co_{NS}@Cu_{PD}$ as the potential negatively shifted (Fig. 5b). It delivers a cathodic current density of − 300 mA cm^{-2} at − 0.22 V, exceeding the start-of-the-art Pt/C catalyst (−300 mA cm^{-2} at −0.234 V, refer to Fig. 2b). Fig. 5c shows the
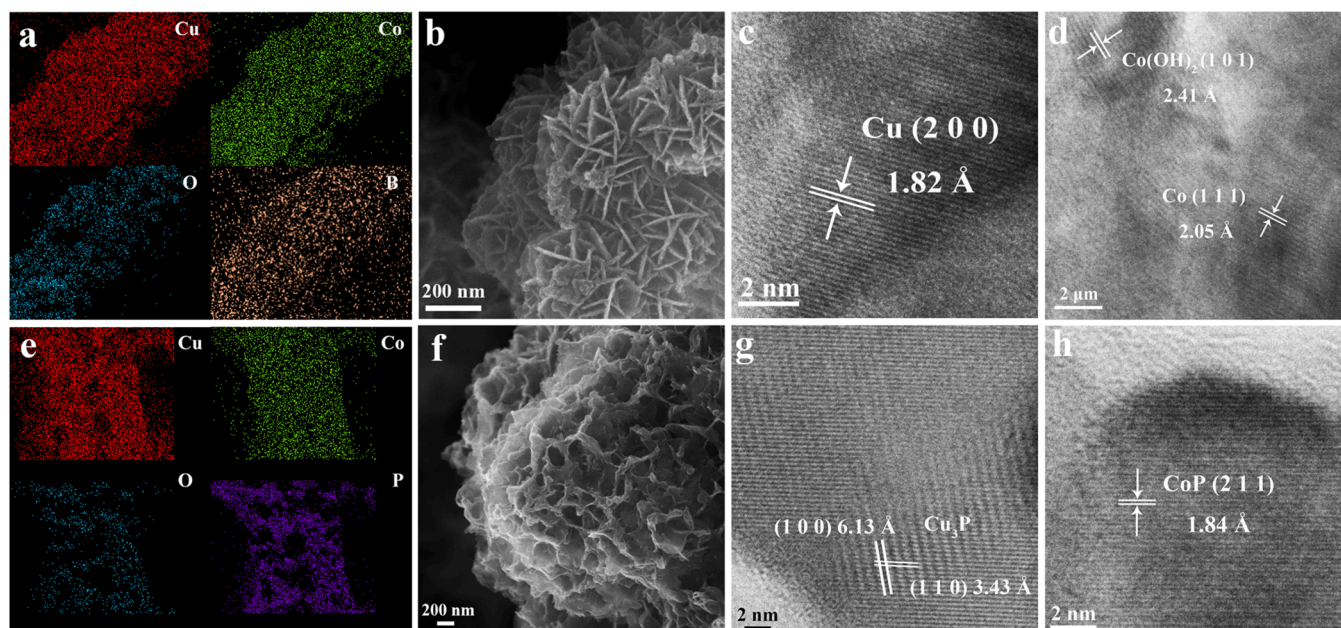
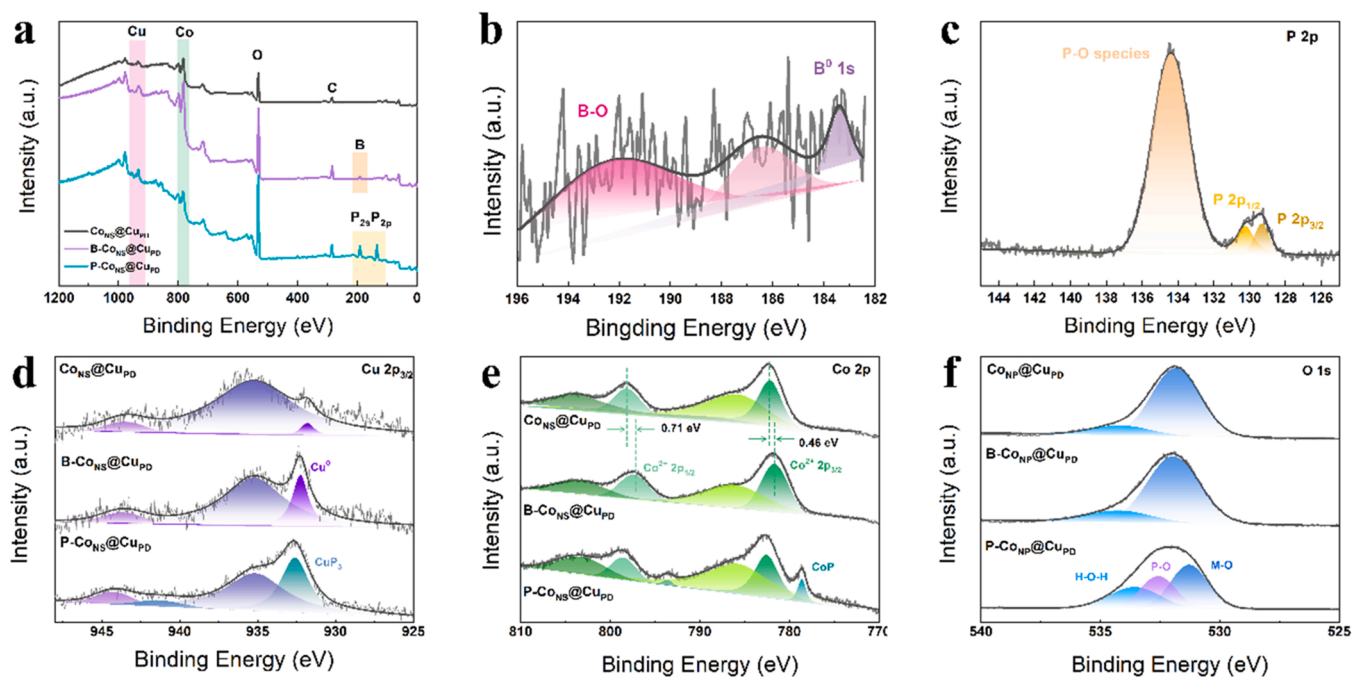**Fig. 3.** The EDS mapping, SEM and HRTEM images of (a–d) B-Co$_{NS}$@Cu$_{PD}$ and (e–h) P-Co$_{NS}$@Cu$_{PD}$.

Fig. 4. (a) XPS survey, (b) B 1s spectrum of B-Co$_{NS}$@Cu$_{PD}$, (c) P 2p spectrum of P-Co$_{NS}$@Cu$_{PD}$, (d) Cu 2p, (e) Co 2p and (f) O 1s XPS spectra of Co$_{NS}$@Cu$_{PD}$ and above two electrodes.

working potential stability of HzOR and HER at a constant current density of $\pm$ 10 mA cm^{-2} for 10 h. The surface morphology and porous structure of the two catalysts unchanged and elemental distribution was still uniform after a 10-h test (Fig. S13). The chemical states of B-Co$_{NS}$@Cu$_{PD}$ and P-Co$_{NS}$@Cu$_{PD}$ exhibit a little change as shown Fig. S14 (see details in Supplementary Information). Thus, both B-Co$_{NS}$@Cu$_{PD}$ and P-Co$_{NS}$@Cu$_{PD}$ proved exceptionally stable during the testing period.

Of the three catalysts Co$_{NS}$@Cu$_{PD}$, B-Co$_{NS}$@Cu$_{PD}$ and P-Co$_{NS}$@Cu$_{PD}$, the Tafel slope of HzOR is in the order of B-Co$_{NS}$@Cu$_{PD}$ < Co$_{NS}$@Cu$_{PD}$ < P-Co$_{NS}$@Cu$_{PD}$ while that of HER is in the reverse order, resulting in a lower dynamic potential region for HzOR on B-Co$_{NS}$@Cu$_{PD}$ (-150 mV) than that of HER on P-Co$_{NS}$@Cu$_{PD}$ (-75 mV) (Fig. 5d). Moreover, the

specific activity of B-Co$_{NS}$@Cu$_{PD}$ for HzOR and P-Co$_{NS}$@Cu$_{PD}$ for HER are also higher than that of Co$_{NS}$@Cu$_{PD}$, suggesting their optimized intrinsic catalytic activity respectively (Fig. S15). These results clearly demonstrate that the intrinsic activities of HzOR and HER are significantly improved by doping B and P into Co$_{NS}$@Cu$_{PD}$, respectively. Even in the low-concentration solutions (1 M KOH-0.1/0.5 M N$_2$H$_4$), B-Co$_{NS}$@Cu$_{PD}$ and P-Co$_{NS}$@Cu$_{PD}$ also show the excellent HzOR and HER performance respectively as shown in Fig. S16. In particular, B-Co$_{NS}$@Cu$_{PD}$ proved superior to electrocatalysts reported to date for HzOR (Table S3). The outstanding performance of B-Co$_{NS}$@Cu$_{PD}$ and P-Co$_{NS}$@Cu$_{PD}$ can likely be attributed to the following factors: exceptionally large electrochemical specific area (ECSA) (B-Co$_{NS}$@Cu$_{PD}$, 747 cm^2 and
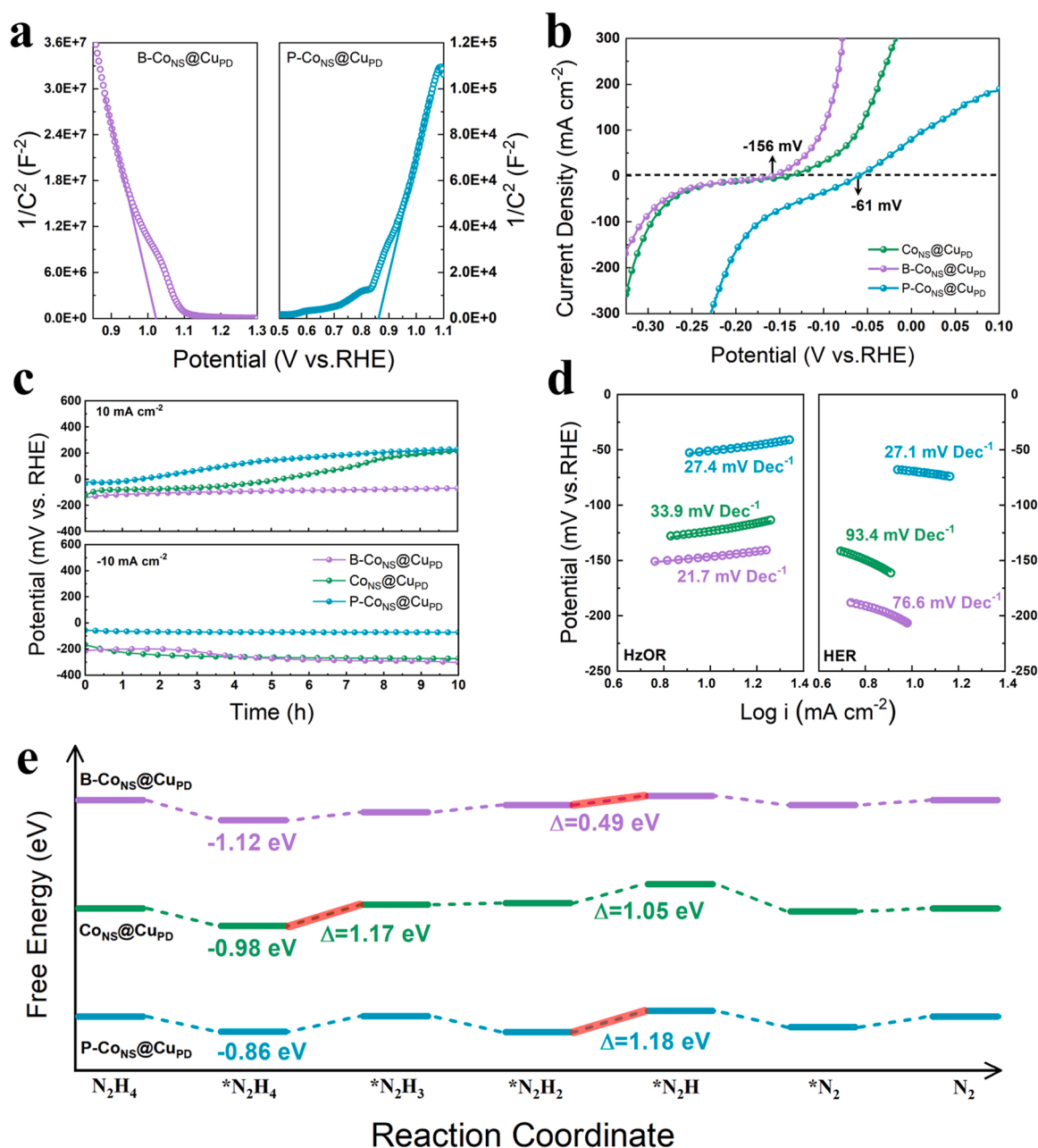
Fig. 5. (a) The Motto-Schottky analysis in Ar-saturated 1 M KOH. (b) LSV curves at a scan rate of 5 mV s^{-1}, (c) durability teats at $\pm$ 10 mA cm^{-2} for 10 h, (d) Tafel slopes for HzOR and HER tested in 3 M KOH-0.1 M N$_2$H$_4$. (e) The free-energy profiles of HzOR of Co$_{NS}$@Cu$_{PD}$, B-Co$_{NS}$@Cu$_{PD}$ and P-Co$_{NS}$@Cu$_{PD}$.

P-Co$_{NS}$@Cu$_{PD}$, 1104 cm^2, see Fig. S17), expressways for electron transfer benefited from the hierarchical porous structure of Co(OH)$_2$ nanosheets grown on microporous Cu dendrites (see Fig. 2d), the p-type semiconductor surface of B-Co$_{NS}$@Cu$_{PD}$ having abundant electron-deficient B sites for the adsorption of *N$_2$H$_x$ and the n-type semiconductor surface of P-Co$_{NS}$@Cu$_{PD}$ having plenty of electron-rich P sites for the adsorption of *H (see DFT calculation and discussion below).

To further understand the effect of B- and P-doping of Co$_{NS}$@Cu$_{PD}$ on the catalytic activities of HzOR and HER, we conducted the DFT calculations for the free energy of the intermediates of HzOR (N$_2$H$_4$ → *N$_2$H$_4$ → *N$_2$H$_3$ → *N$_2$H$_2$ → *N$_2$H → *N$_2$ → N$_2$) on the Co planes of Co(OH)$_2$ (0 0 1), Co (1 1 1) and CoP (2 1 1) in accordance with the HRTEM and XPS characterization (Figs. 1, 3 and 4). The optimized atomic structure models (Fig. S18) of the three catalysts were employed for the DFT calculation. The most stable configurations for each intermediate adsorbed on the catalyst are shown in Fig. S19 and the free energy

diagram for the adsorption and dehydrogenation process of N$_2$H$_4$ are shown in Fig. 5e. The first dehydrogenation of the process (*N$_2$H$_4$ → *N$_2$H$_3$) is the rate-determining step (ΔG = 1.17 eV) and the third dehydrogenation (*N$_2$H$_2$ → *N$_2$H) is the second energy barrier for HzOR on Co$_{NS}$@Cu$_{PD}$. By contrast, the third dehydrogenation (*N$_2$H$_2$ → *N$_2$H) is the rate-determining step on B-Co$_{NS}$@Cu$_{PD}$ and the energy barrier of HzOR catalyzed by B-Co$_{NS}$@Cu$_{PD}$ is significantly reduced (ΔG = 0.49 eV). When P-Co$_{NS}$@Cu$_{PD}$ is used for HzOR, the third dehydrogenation (*N$_2$H$_2$ → *N$_2$H) is still the rate-determining step, but its energy barrier reaches 1.18 eV. Clearly, the DFT calculation is in a good agreement with the experimental results, i.e., the HzOR performance is in the order of B-Co$_{NS}$@Cu$_{PD}$ > Co$_{NS}$@Cu$_{PD}$ > P-Co$_{NS}$@Cu$_{PD}$ (refer to Fig. 5b). As for HER, the Gibbs free energy for H* on P-Co$_{NS}$@Cu$_{PD}$ (ΔG$_{H*}$ = − 0.10 eV) is closer to zero than that on Co$_{NS}$@Cu$_{PD}$ (− 0.26 eV) while the ΔG$_{H*}$ on B-Co$_{NS}$@Cu$_{PD}$ increased to − 0.34 eV (Fig. S20).

The above results confirm that the p-type semiconductor electrocatalyst (B-Co_{NS}@Cu_{PD}) prefers the anodic reaction of HzOR and the n-type semiconductor (P-Co_{NS}@Cu_{PD}) is conducive to the cathodic HER. To further demonstrate the viability of the p- and n-type semiconductors, we compared B-Co_{NS}@Cu_{PD} and P-Co_{NS}@Cu_{PD} with doped and undoped Co_{NS} and Cu_{PD} for the catalytic activities of HzOR and HER (Fig. S21). Indeed, doping B and P into Co_{NS} and Cu_{PD} improved their HzOR and the HER activity, respectively. Nevertheless, the improvement of the anodic HzOR by doping P into Co_{NS} (n-type semiconductors) and that of the cathodic HER by doping B into Co_{NS} (p-type semiconductors) were likely attributed to enhanced surface conductivity of $Co(OH)_2$ nanosheets. Clearly, B- and P-doped Co_{NS}@Cu_{PD} are the best HzOR and HER electrocatalysts, respectively.

3.3. Co-generation of H_2 and electricity by hydrazine assisted water electrolysis

The working potential of HzOR on B-Co_{NS}@Cu_{PD} and that of HER on P-Co_{NS}@Cu_{PD} at ± 10 mA cm^{-2} are -146 and -70 mV, respectively (Fig. 5b, c), indicating that $E_{HzOR} < E_{HER}$ has been achieved in a homogeneous hydrazine solution in the three-electrode system. Most significantly, the two-electrode hydrazine-assisted water electrolysis device of P-Co_{NS}@Cu_{PD} || B-Co_{NS}@Cu_{PD} produced a current density of 28 mA cm^{-2} at 0 V (Fig. 6a) while generating H_2 (Fig. S22). Notably, at a hydrogen production current of 10 mA cm^{-2}, the device outputs a small voltage of 60 mV achieving the co-generation of H_2 and electricity. While the chronopotentiometry curves show that the Pt/C || Pt/C and Co_{NS}@Cu_{PD} || Co_{NS}@Cu_{PD} devices require an input voltage of 98 and 54 mV at 10 mA cm^{-2}, respectively (Fig. 6b). However, the output voltage of 60 mV decreased slowly with time and eventually approached zero as the hydrazine was consumed (Fig. 6b). The electrolysis performance was restored almost to its original level by renewing the electrolyte solution. B-Co_{NS}@Cu_{PD} and P-Co_{NS}@Cu_{PD} outperform the catalysts for HzE reported in the literature under comparable conditions (Table S4).

B-Co_{NS}@Cu_{PD} and P-Co_{NS}@Cu_{PD} were also applied to the electrolysis of $NaBH_4$ and $NH_3\cdot BH_3$ solutions (Fig. S23). The $NaBH_4$- and $NH_3\cdot BH_3$-assisted water electrolysis devices produced a current of 36 mA cm^{-2} and 3.6 mA cm^{-2} respectively, without applying electric power meanwhile generating hydrogen. By contrast, the overall water electrolysis in 3 M KOH almost shown no response during the whole test range and it required an input voltage of 1.68 V at 10 mA cm^{-2} (Fig. S24), implying the hydrogen-rich molecule-assisted water electrolysis is indeed an effective method to greatly decrease the voltage of hydrogen production. Furthermore, the Co_{NS}@Cu_{PD} was also doped with S (Fig. S25a-c)

which create a n-type semiconductor surface (Fig. S25d) and improve the HER activity (Fig. S25e, f). The two-electrode HzE device of S-Co_{NS}@Cu_{PD} || B-Co_{NS}@Cu_{PD} achieved an output of 5 mA cm^{-2} at 0 V for hydrogen generation (Fig. S25g). This is the first reported work about outputting electricity and hydrogen simultaneously. Even the output cell voltage in this work is indeed low, it could be improved by further developing advance electrocatalysts in the future work.

4. Conclusions

In summary, Co_{NS}@Cu_{PD} with hierarchical porous structure was prepared through a simple and rapid two-step electrodeposition method. Through the B-/P-doping to adjust the HzOR/HER intrinsic activity of Co_{NS}@Cu_{PD} contrarily, the working potential for HzOR on B-Co_{NS}@Cu_{PD} is optimized to be lower than that for HER on P-Co_{NS}@Cu_{PD}. Notably, the hydrazine-assisted water electrolysis device using P-Co_{NS}@Cu_{PD} || B-Co_{NS}@Cu_{PD} achieves co-generation of hydrogen and electricity (outputting 60 mV at 10 mA cm^{-2}). The unique hierarchical porous structure operates as an express highway for electron transport improving the conductivity and eliminating the accumulation of electrons at the electrode-electrolyte interface. The B-/P-doping creates abundant defects and active sites and is a visualization of "pushing and pulling" the electronic state in an opposite direction, i.e., the electron-deficient state to preferentially adsorb the electron-rich N sites of N_2H_4 to facilitate HzOR and the electron-rich state to adsorb the electron-deficient H sites of H_2O to facilitate HER. This work lights an interesting strategy of modulating the electronic structure and adsorption characteristic selectively to fabricate the targeted and efficient electrocatalysts for electricity-independent hydrogen-rich molecule-assisted electrochemical hydrogen production.

CRediT authorship contribution statement

Shuxian Zhuang: Methodology, Formal analysis, Investigation, Data curation, Writing – original draft, Writing – review & editing. **Yang Tang:** Conceptualization, Methodology, Writing – review & editing, Project administration, Funding acquisition. **Xuefeng Tai:** Methodology, Calculation. **Qian Huang:** Data curation. **Pingyu Wan:** Conceptualization, Supervision, Project administration. **Yongmei Chem:** Supervision, Funding acquisition. **Yanzhi Sun:** Validation. **Junqing Pan:** Validation. **Xiao Jin Yang:** Conceptualization, Writing – review & editing, Validation, Supervision. All authors reviewed and commented on the manuscript before publication.
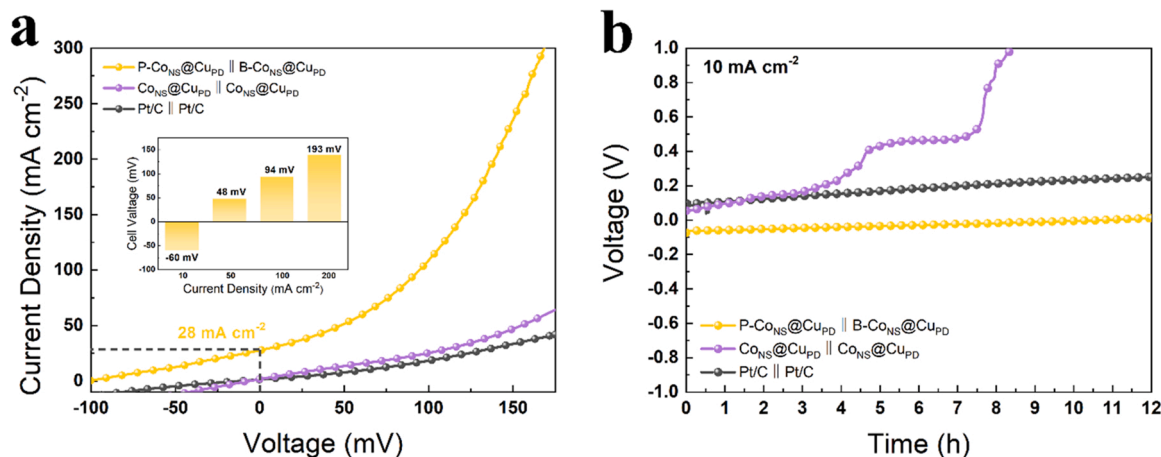

Fig. 6. (a) The LSV curves and (b) durability tests at 10 mA cm^{-2} in 3 M KOH-0.1 M N_2H_4 of two-electrode HzE devices. The inset is the cell voltages of P-Co_{NS}@Cu_{PD} || B-Co_{NS}@Cu_{PD} at 10, 50, 100 and 200 mA cm^{-2}.

Declaration of Competing Interest

The authors declare that they have no known competing financial interests or personal relationships that could have appeared to influence the work reported in this paper.

Acknowledgments

Appendix A. Supporting information

Supplementary data associated with this article can be found in the online version at doi:10.1016/j.apcatb.2022.121132.

References

[1] I. Staffell, D. Scamman, A. Velazquez Abad, P. Balcombe, P.E. Dodds, P. Ekins, N. Shah, K.R. Ward, The role of hydrogen and fuel cells in the global energy system, Energy Environ. Sci. 12 (2019) 463–491.

[2] O.J. Guerra, J. Eichman, J. Kurtz, B.-M. Hodge, Cost competitiveness of electrolytic hydrogen, Joule 3 (2019) 2425–2443.

[3] G. Glenk, S. Reichelstein, Economics of converting renewable power to hydrogen, Nat. Energy 4 (2019) 216–222.

[4] X. Zou, Y. Zhang, Noble metal-free hydrogen evolution catalysts for water splitting, Chem. Soc. Rev. 44 (2015) 5148–5180.

[5] P. Zhai, Y. Zhang, Y. Wu, J. Gao, B. Zhang, S. Cao, Y. Zhang, Z. Li, L. Sun, J. Hou, Engineering active sites on hierarchical transition bimetal oxides/sulfides heterostructure array enabling robust overall water splitting, Nat. Commun. 11 (2020) 5462.

[6] H. Dotan, G.E. Shter, D.A. Grave, N. Hadari, C. Cohen, A. Landman, S.W. Sheehan, Z. Arzi, A. Rothschild, K.D. Malviya, N. Yehudai, M. Halabi, N. Gal, G.S. Grader, Decoupled hydrogen and oxygen evolution by a two-step electrochemical–chemical cycle for efficient overall water splitting, Nat. Energy 4 (2019) 786–795.

[7] Y.P. Zhu, T.Y. Ma, M. Jaroniec, S.Z. Qiao, Self-templating synthesis of hollow Co₃O₄ microtube arrays for highly efficient water electrolysis, Angew. Chem. Int. Ed. 56 (2017) 1324–1328.

[8] Z.-P. Wu, X.F. Lu, S.-Q. Zang, X.W.D. Lou, Non-noble-metal-based electrocatalysts toward the oxygen evolution reaction, Adv. Funct. Mater. 30 (2020), 1910274.

[9] F. Dionigi, Z. Zeng, I. Sinev, T. Merzdorf, S. Deshpande, M.B. Lopez, S. Kunze, I. Zegkinoglou, H. Sarodnik, D. Fan, A. Bergmann, J. Drnec, J.F. Araujo, M. Gliech, D. Teschner, J. Zhu, W.X. Li, J. Greeley, B.R. Cuenya, P. Strasser, In-situ structure and catalytic mechanism of NiFe and CoFe layered double hydroxides during oxygen evolution, Nat. Commun. 11 (2020) 2522.

[10] M. Liu, R. Zhang, L. Zhang, D. Liu, S. Hao, G. Du, A.M. Asiri, R. Kong, X. Sun, Energy-efficient electrolytic hydrogen generation using a Cu₃P nanoarray as a bifunctional catalyst for hydrazine oxidation and water reduction, Inorg. Chem. Front. 4 (2017) 420–423.

[11] A. Tiwari, V. Singh, T.C. Nagaiah, Non-noble cobalt tungstate catalyst for effective electrocatalytic oxidation of borohydride, ACS Appl. Mater. Interface 11 (2019) 21465–21472.

[12] J.-Y. Zhang, T. He, M. Wang, R. Qi, Y. Yan, Z. Dong, H. Liu, H. Wang, B.Y. Xia, Energy-saving hydrogen production coupling urea oxidation over a bifunctional nickel-molybdenum nanotube array, Nano Energy 60 (2019) 894–902.

[13] C. Wu, J. Zhu, H. Wang, G. Wang, T. Chen, Y. Tan, Porous Ni₁₋ₓCuₓO nanowire arrays as noble-metal-free high-performance catalysts for ammonia-borane electrooxidation, ACS Catal. 10 (2019) 721–735.

[14] D.Cd Oliveira, W.O. Silva, M. Chatenet, F.H.B. Lima, NiOₓ-Pt/C nanocomposites: Highly active electrocatalysts for the electrochemical oxidation of hydrazine, Appl. Catal. B-Environ. 201 (2017) 22–28.

[15] Yi Liu, Jihua Zhang, Yapeng Li, Qizhu Qian, Ziyun Li, Yin Zhu, Genqiang Zhang, Manipulating dehydrogenation kinetics through dual-doping Co₃N electrode enables highly efficient hydrazine oxidation assisting self-powered H₂ production, Nat. Commun. 11 (2020) 1853.

[16] X. Liu, J. He, S. Zhao, Y. Liu, Z. Zhao, J. Luo, G. Hu, X. Sun, Y. Ding, Self-powered H₂ production with bifunctional hydrazine as sole consumable, Nat. Commun. 9 (2018) 4365.

[17] T. Sakamoto, H. Kishi, S. Yamaguchi, D. Matsumura, K. Tamura, A. Hori, Y. Horiuchi, A. Serov, K. Artyushkova, P. Atanassov, H. Tanaka, Mechanism study of hydrazine electrooxidation reaction on nickel oxide surface in alkaline electrolyte by in situ XAFS, J. Electrochem. Soc. 163 (2016) H951–H957.

[18] Z. Pu, I.S. Amiinu, F. Gao, Z. Xu, C. Zhang, W. Li, G. Li, S. Mu, Efficient strategy for significantly decreasing overpotentials of hydrogen generation via oxidizing small molecules at flexible bifunctional CoSe electrodes, J. Power Sources 401 (2018) 238–244.

[19] M. Du, H. Sun, H. Li, X. Ye, F. Yue, J. Yang, Y. Liu, F. Guo, Integrative Ni@Pd-Ni alloy nanowire array electrocatalysts boost hydrazine oxidation kinetics, ChemElectroChem 6 (2019) 5581–5587.

[20] T. Wang, G.-R. Xu, H.-Y. Sun, H. Huang, F. Li, P. Chen, Y. Chen, Anodic hydrazine electrooxidation boosted overall water electrolysis by bifunctional porous nickel phosphide nanotubes on nickel foam, Nanoscale 12 (2020) 11526–11535.

[21] Z. Wang, L. Xu, F. Huang, L. Qu, J. Li, K.A. Owusu, Z. Liu, Z. Lin, B. Xiang, X. Liu, K. Zhao, X. Liao, W. Yang, Y.B. Cheng, L. Mai, Copper-nickel nitride nanosheets as efficient bifunctional catalysts for hydrazine-assisted electrolytic hydrogen production, Adv. Energy Mater. 9 (2019), 1900390.

[22] J.-Y. Zhang, H. Wang, Y. Tian, Y. Yan, Q. Xue, T. He, H. Liu, C. Wang, Y. Chen, B.Y. Xia, Anodic hydrazine oxidation assists energy-efficient hydrogen evolution over a bifunctional cobalt perselenide nanosheet electrode, Angew. Chem. Int. Ed. 57 (2018) 7649–7653.

[23] X. Xiao, S. Liu, D. Huang, X. Lv, M. Li, X. Jiang, L. Tao, Z. Yu, Y. Shao, M. Wang, Y. Shen, Highly efficient hydrogen production using a reformed electrolysis system driven by a single perovskite solar cell, ChemSusChem 12 (2019) 434–440.

[24] G. Wang, J. Chen, P. Cai, J. Jia, Z. Wen, A self-supported Ni-Co perselenide nanorod array as a high-activity bifunctional electrode for a hydrogen-producing hydrazine fuel cell, J. Mater. Chem. A 6 (2018) 17763–17770.

[25] Z. Zhang, G. Liu, X. Cui, Y. Gong, D. Yi, Q. Zhang, C. Zhu, F. Saleem, B. Chen, Z. Lai, Q. Yun, H. Cheng, Z. Huang, Y. Peng, Z. Fan, B. Li, W. Chen, Y. Du, L. Ma, C.-J. Sun, I. Hwang, S. Chen, L. Song, F. Ding, L. Gu, Y. Zhu, H. Zhang, Evoking ordered vacancies in metallic nanostructures toward a vacated Barlow packing for high-performance hydrogen evolution, Sci. Adv. 7 (2021) eabd6647.

[26] Y. Xie, Q. Qian, J. Zhang, J. Li, Y. Li, X. Jin, Y. Zhu, Y. Liu, Z. Li, A. El-Harairy, C. Xiao, G. Zhang, Artificial heterointerfaces achieve delicate reaction kinetics towards hydrogen evolution and hydrazine oxidation catalysis, Angew. Chem. Int. Ed. 60 (2020) 5984–5993.

[27] M. Li, Z. Zhang, H. Xiong, L. Wang, S. Zhuang, M.D. Argyle, Y. Tang, X. Yang, Y. Chen, P. Wan, M. Fan, 0.03 V electrolysis voltage driven hydrazine assisted hydrogen generation on NiCo phosphide nanowires supported nicohydroxide nanosheets, ChemElectroChem 7 (2020) 3089–3097.

[28] Y. Li, J. Zhang, Y. Liu, Q. Qian, Z. Li, Y. Zhu, G. Zhang, Partially exposed RuP₂ surface in hybrid structure endows its bifunctionality for hydrazine oxidation and hydrogen evolution catalysis, Sci. Adv. 6 (2020) eabb4197.

[29] G. Kresse, J. Furthmiiller, Efficiency of ab-initio total energy calculations for metals and semiconductors using a plane-wave basis set, Comput. Mater. Sci. 6 (1996) 15–50.

[30] G. Kresse, J. Furthmuller, Efficient iterative schemes for ab initio total-energy calculations using a plane-wave basis set, Phys. Rev. B 54 (1996) 11169–11186.

[31] J.P. Perdew, K. Burke, M. Ernzerhof, Generalized gradient approximation made simple, Phys. Rev. Lett. 77 (1996) 3865–3868.

[32] G. Kresse, D. Joubert, From ultrasoft pseudopotentials to the projector augmented-wave method, Phys. Rev. B 59 (1999) 1758–1775.

[33] P.E. Blochl, Projector augmented-wave method, Phys. Rev. B 50 (1994) 17953–17979.

[34] S. Grimme, J. Antony, S. Ehrlich, H. Krieg, A consistent and accurate ab initio parametrization of density functional dispersion correction (DFT-D) for the 94 elements H-Pu, J. Chem. Phys. 132 (2010), 154104.

[35] D. Nam, R. Kim, D. Han, J. Kim, H. Kwon, Effects of (NH₄)₂SO₄ and BTA on the nanostructure of copper foam prepared by electrodeposition, Electrochim. Acta 56 (2011) 9397–9405.

[36] H. Xu, J.-X. Feng, Y.-X. Tong, G.-R. Li, Cu₂O-Cu hybrid foams as high-performance electrocatalysts for oxygen evolution reaction in alkaline media, ACS Catal. 7 (2016) 986–991.

[37] S. Zhuang, S. Tong, H. Wang, H. Xiong, Y. Gong, Y. Tang, J. Liu, Y. Chen, P. Wan, The P/NiFe doped NiMoO₄ micro-pillars arrays for highly active and durable hydrogen/oxygen evolution reaction towards overall water splitting, Int. J. Hydrogen Energy 44 (2019) 24546–24558.

[38] Y. He, Q. He, L. Wang, C. Zhu, P. Golani, A.D. Handoko, X. Yu, C. Gao, M. Ding, X. Wang, F. Liu, Q. Zeng, P. Yu, S. Guo, B.I. Yakobson, L. Wang, Z.W. Seh, Z. Zhang, M. Wu, Q.J. Wang, H. Zhang, Z. Liu, Self-gating in semiconductor electrocatalysis, Nat. Mater. 18 (2019) 1098–1104.

[39] H. Jiang, Z. Wang, P. Kannan, H. Wang, R. Wang, P. Subramanian, S. Ji, Grain boundaries of Co(OH)₂-Ni-Cu nanosheets on the cotton fabric substrate for stable and efficient electro-oxidation of hydrazine, Int. J. Hydrogen Energy 44 (2019) 24591–24603.

[40] R. Zhang, X. Wang, S. Yu, T. Wen, X. Zhu, F. Yang, X. Sun, X. Wang, W. Hu, Ternary NiCo₂Pₓ nanowires as pH-universal electrocatalysts for highly efficient hydrogen evolution reaction, Adv. Mater. 29 (2017), 1605502.

[41] Q. Huang, S. Zhuang, X. You, J. Zhang, A. Xie, Y. Chen, Y. Tang, Y. Chen, M. Shao, X.J. Yang, P. Wan, Honeycomb-like carbon with doping of a transition-metal and nitrogen for highly efficient zinc–air battery and zinc-ion battery, Sustain. Energy Fuels 6 (2022) 188–196.

[42] C.-C. Yang, M.-S. Chen, Y.-W. Chen, Hydrogen generation by hydrolysis of sodium borohydride on CoB/SiO₂ catalyst, Int. J. Hydrogen Energy 36 (2011) 1418–1423.

[43] W. Lu, T. Liu, L. Xie, C. Tang, D. Liu, S. Hao, F. Qu, G. Du, Y. Ma, A.M. Asiri, X. Sun, In situ derived Co-B nanoarray: a high-efficiency and durable 3D bifunctional electrocatalyst for overall alkaline water splitting, Small 13 (2017), 1700805.

[44] N. Patel, A. Miotello, Progress in Co-B related catalyst for hydrogen production by hydrolysis of boron-hydrides: a review and the perspectives to substitute noble metals, Int. J. Hydrogen Energy 40 (2015) 1429–1464.

[45] K. Jiang, K. Xu, S. Zou, W.-B. Cai, B-doped Pd catalyst: boosting room-temperature hydrogen production from formic acid-formate solutions, J. Am. Chem. Soc. 136 (2014) 4861–4864.

[46] X. Yu, P. Han, Z. Wei, L. Huang, Z. Gu, S. Peng, J. Ma, G. Zheng, Boron-doped graphene for electrocatalytic N₂ reduction, Joule 2 (2018) 1610–1622.

[47] H. Du, X. Zhang, Q. Tan, R. Kong, F. Qu, A. Cu$_3$P-CoP, hybrid nanowire array: a superior electrocatalyst for acidic hydrogen evolution reactions, Chem. Commun. 53 (2017) 12012–12015.

[48] T. Liu, K. Wang, G. Du, A.M. Asiric, X. Sun, Self-supported CoP nanosheet arrays: a non-precious metal catalyst for efficient hydrogen generation from alkaline NaBH$_4$ solution, J. Mater. Chem. A 4 (2016) 13053–13057.

[49] J. Tian, Q. Liu, N. Cheng, A.M. Asiri, X. Sun, Self-supported Cu$_3$P nanowire arrays as an integrated high-performance three-dimensional cathode for generating hydrogen from water, Angew. Chem. Int. Ed. 53 (2014) 9577–9581.

[50] K. Xu, H. Cheng, H. Lv, J. Wang, L. Liu, S. Liu, X. Wu, W. Chu, C. Wu, Y. Xie, Controllable surface reorganization engineering on cobalt phosphide nanowire arrays for efficient alkaline hydrogen evolution reaction, Adv. Mater. 30 (2018), 1703322.

[51] Hong Bin Yang, Jianwei Miao, Sung-Fu Hung, Jiazang Chen, Hua Bing Tao, Xizu Wang, Liping Zhang, Rong Chen, Jiajian Gao, Hao Ming Chen, Liming Dai, B. Liu, Identification of catalytic sites for oxygen reduction and oxygen evolution in N-doped graphene materials: development of highly efficient metal-free bifunctional electrocatalyst, Sci. Adv. 2 (2016), e1501122.

[52] J. Hou, Y. Sun, Y. Wu, S. Cao, L. Sun, Promoting active sites in core-shell nanowire array as Mott-Schottky electrocatalysts for efficient and stable overall water splitting, Adv. Funct. Mater. 28 (2018), 1704447.